Bioconjugate Chemistry

Article

Cite This: Bioconjugate Chem. 2018, 29, 3833−3840

pubs.acs.org/bc

Molecular Targeted NIR-II Probe for Image-Guided Brain Tumor Surgery

Sorel Kurbegovic,[†,‡] Karina Juhl,[‡] Hao Chen,[†] Chunrong Qu,[†] Bingbing Ding,[†] Julie Maja Leth,[§,⊥] Krzysztof Tadeusz Drzewiecki,[∥] Andreas Kjaer,*[,‡] and Zhen Cheng*[,†]

[†]Molecular Imaging Program at Stanford (MIPS), Bio-X Program, and Department of Radiology, Canary Center at Stanford for Cancer Early Detection, Stanford University, Stanford, California, 94305-5344, United States

[‡]Department of Clinical Physiology, Nuclear Medicine & PET and Cluster for Molecular Imaging, Department of Biomedical Sciences, Rigshospitalet and University of Copenhagen, 2200 Copenhagen N, Denmark

[§]Finsen Laboratory, Rigshospitalet, 2200 Copenhagen N, Denmark

[⊥]Biotech Research and Innovation Centre (BRIC), University of Copenhagen, 2200 Copenhagen N, Denmark

[∥]Department of Plastic Surgery, Breast Surgery and Burns Treatment, Rigshospitalet and University of Copenhagen, 2100 Copenhagen Ø, Denmark

ABSTRACT: Optical imaging strategies for improving delineation of glioblastoma (GBM) is highly desired for guiding surgeons to distinguish cancerous tissue from healthy and precious brain tissue. Fluorescence imaging (FLI) in the second near-infrared window (NIR-II) outperforms traditional NIR-I imaging with better tissue penetration, higher spatial and temporal resolution, and less auto fluorescence and scattering. Because of high expression in GBM and many other tumors, urokinase Plasminogen Activator Receptor (uPAR) is an attractive and well proven target for FLI. Herein we aim to combine the benefit of a NIR-II fluorophore with a high affinity uPAR targeting small peptide. A targeted NIR-II fluorescent probe was developed by conjugating an in-house synthesized NIR-II fluorophore, CH1055, and a uPAR targeting peptide, AE105. To characterize the *in vivo* distribution and targeting properties, a dynamic imaging was performed in orthotopic GBM bearing nude mice (n = 8). Additionally, fluorescence guided surgery of orthotopic GBM was performed in living animals. CH1055-4Glu-AE105 was easily synthesized with >75% yield and >98% HPLC evaluated purity. The retention time of the probe on analytical HPLC was 15.9 min and the product was verified by mass spectrometry. Dynamic imaging demonstrated that the uPAR targeting probe visualized orthotopic GBM through the intact skull with a tumor-to-background ratio (TBR) of 2.7 peaking at 96 h. Further, the orthotopic GBM was successfully resected in small animals guided by the NIR-II FLI. By using a small uPAR targeting NIR-II probe, FLI allows us to specifically image and detect GBM. A real-time imaging setup further renders FLI guided tumor resection, and the probe developed in this work is a promising candidate for clinical translation.

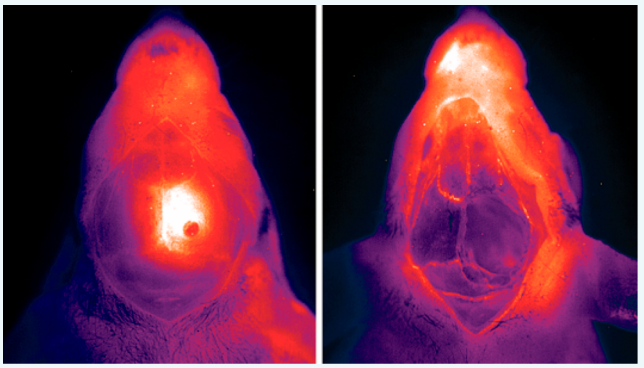

INTRODUCTION

Accurate visualization of cancer tissue can help surgeons during surgery to delineate diseased tissue from healthy tissue. Glioblastoma (GBM) is a heterogenic, complex and serious illness with a fatal outcome and in essence no cure. Even with aggressive treatment the median survival is only 15 months.[1] For the last 10−15 years, GBM management has been stagnant with only modest progress in treatment strategies, and currently there is no curative treatment for patients suffering from the disease. Thus, better GBM management is needed and relies on both oncological and surgical improvements.

Positive resection margins in cancer surgery are related to higher risk of tumor recurrence with poor postoperative prognosis in several cancers including GBM.[2,3] The infiltrative nature of GBM makes it hard to visualize and distinguish from healthy brain tissue in white light making it practically impossible to resect accurately without leaving any tumor tissue. Usually, anatomical location and extension of the tumor are mapped preoperatively on computed tomography (CT) and/or magnetic resonance imaging (MRI) and incorporated into a stereotactic navigation guided surgery. However, intraoperative brain shift during neurosurgical procedures is a well-known phenomenon caused by gravity, tissue manipulation, tumor type and size, fluid loss, and use of medication leading to a mismatch between the preoperative imaging and the actual intraoperative tumor location.[4,5] Thus, the main drawbacks of preoperative CT or MRI continue to be the lack

Received: September 24, 2018
Published: October 8, 2018

DOI: 10.1021/acs.bioconjchem.8b00669
Bioconjugate Chem. 2018, 29, 3833−3840

of intraoperative real-time imaging, and accurate visualization of the biological extent of the cancer with the infiltrative tendrils of GBM.

Optical imaging, in contrast, enables noninvasive real-time *in vivo* visualization with high temporal and spatial resolution without exposing the living subjects to ionizing radiation as with X-rays used in CT. Thus, it can be used for safe, long, and repeated visualization of living organisms and tissue with no harmful effects. Optical imaging strategies for improving delineation of GBM is highly desired for guiding surgeons to identify and resect cancerous tissue to achieve a negative resection margin while at the same time sparing healthy and precious brain tissue. Although surgical treatment probably cannot stand alone in the treatment, advances in targeted tumor visualization and delineation for surgical guidance is necessary to achieve complete resection and might increase the postoperative survival. Optical imaging is currently possible by Raman spectroscopy, bioluminescence, and fluorescence imaging among others. Raman spectroscopy, in particular, has a potential for *in vivo* imaging with the ability to image multiple targets simultaneously (multiplexing). However, the weak Raman effect, limitations to small sample regions, and lack of a comprehensive, real-time view of the surgical field limits the biomedical application.

Fluorescent probes for *in vivo* optical imaging are an emerging technology that can accurately visualize tumors such as GBM, breast cancer, head and neck squamous cell carcinoma (HNSCC), hepatocellular carcinoma,[6,7] and so forth and can even visualize residual cells during surgery. Currently, four fluorophores, methylene blue,[8] fluorescein sodium,[9] indocyanine green (ICG),[10] and 5-aminolevulinic acid (5-ALA),[11] have been approved for human use by the Food and Drug Administration (FDA) (methylene blue has been used before formal FDA approval was required), and many others have been developed and tested in clinical and preclinical settings.[11] Most of these probes have short emission wavelengths in the visible spectrum (390−650 nm) or in the first near-infrared window (NIR-I, 650−950 nm) limiting the penetration (~0.2 mm depth), resolution, and tumor-to-background ratio due to auto fluorescence, light absorption, and scattering. On the contrary, fluorescence imaging (FLI) in the second near-infrared window (NIR-II, 1000−1700 nm) outperforms the NIR-I window imaging with deeper tissue penetration (~3 mm depth), higher spatial and temporal resolution, as well as less auto fluorescence and scattering.[12−14]

Urokinase plasminogen activator receptor (uPAR) is an attractive and well proven target for molecular imaging in GBM[15,16] and other cancers such as breast cancer and HNSCC,[17−20] since it is overexpressed in the tumor with high intensity at the invading front while the expression in the normal tissue is negligible.[21,22] AE105 is a small uPAR specific peptide[23] and has been proven useful in targeted PET-imaging in humans.[24,25] Herein we aim to combine the benefits from the NIR-II FLI with the high affinity small peptide AE105 into uPAR targeted NIR-II FLI for surgical guidance that may solve some of the limitations of NIR-I imaging and Raman spectroscopy.

RESULTS

Biochemistry and Optical Properties. CH1055-4Glu-AE105 was easily synthesized in >75% yield and >98% HPLC assessed purity. The single peak retention time of CH-4Glu-AE105 on analytical HPLC was 15.9 min and the matrix assisted laser desorption ionization-time-of-flight mass spectrometry (MALDI-TOF-MS) measured molecular weight (MW) was consistent with the expected MW: m/z = 2693 Da for $[M]^+$ for CH1055-4Glu-Asp-Cha-Phe-(D)ser-(D)arg-Tyr-Leu-Trp-Ser-$CONH_2$ (calculated $[M]^+$ = 2693 Da) (Figure 1).

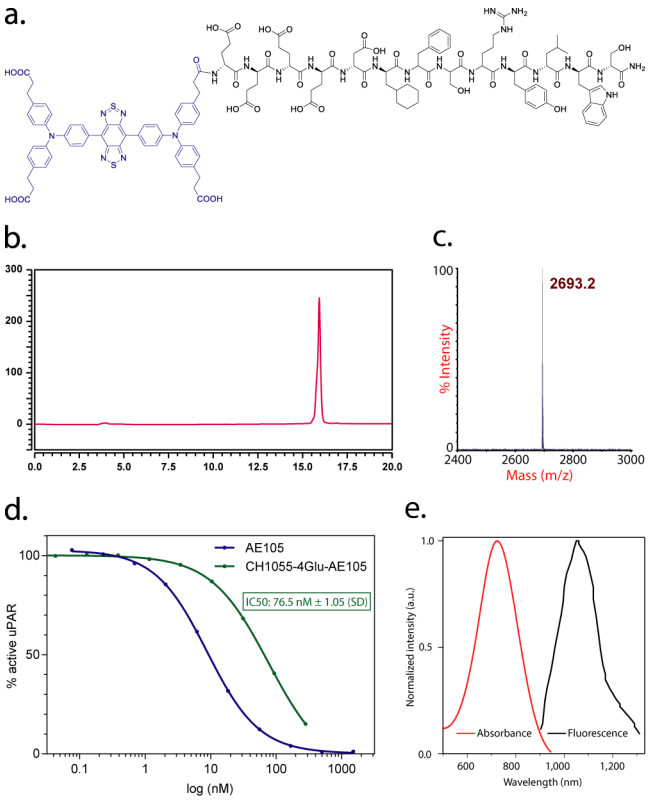

Figure 1. (a) Peptide sequence and schematic molecular structure of CH1055-4Glu-AE105; (b) analytical HPLC of purified probe; (c) MALDI-TOF mass spectrum of CH1055-4Glu-AE105; (d) affinity to the uPAR receptor for the NIR-II labeled peptide (CH1055-4Glu-AE105) and the nonlabeled peptide (AE105); (e) absorbance and fluorescent emission of CH1055, demonstrating an absorbance peak at ~750 nm and an emission peak at ~1055 nm. The fluorescent emission spectrum was obtained with an 808 nm excitation laser.

Binding affinity of the fluorescent labeled AE105 peptide to the uPAR was preserved with IC50 = 76.5 ± 1.05 (SD) (Figure 1d).

In Vivo Imaging. In orthotopic GBM the "through-skull" TBR was 2.7 peaking at 96 h. In contrast, competitively blocked mice showed a TBR of 1.4 (p = 0.002) (Figure 2). On side-by-side comparison with a corresponding NIR-I-AE105 probe, the tumor was clearly more demarcated on "through-skull" visualization with the NIR-II technology compared with NIR-I and quantification showed TBR 2.7 vs 1.4, respectively.

Image-Guided Surgery. Additionally, GBM resections were performed under the guidance of NIR-II imaging. On bright field images, no GBM could not be clearly recognized through the midline incision at the scalp (Figure 3). In contrast, when imaged with NIR-II, the tumor was clearly visualized with clear delineation with TBR = 2.1 between the central tumor and the adjacent tissue (Figure 3). Based on FLI, a complete resection was considered, because of a margin-to-background ratio (MBR) = 1.0 (margin signal 36,000 Gray and

DOI: 10.1021/acs.bioconjchem.8b00669
Bioconjugate Chem. 2018, 29, 3833−3840

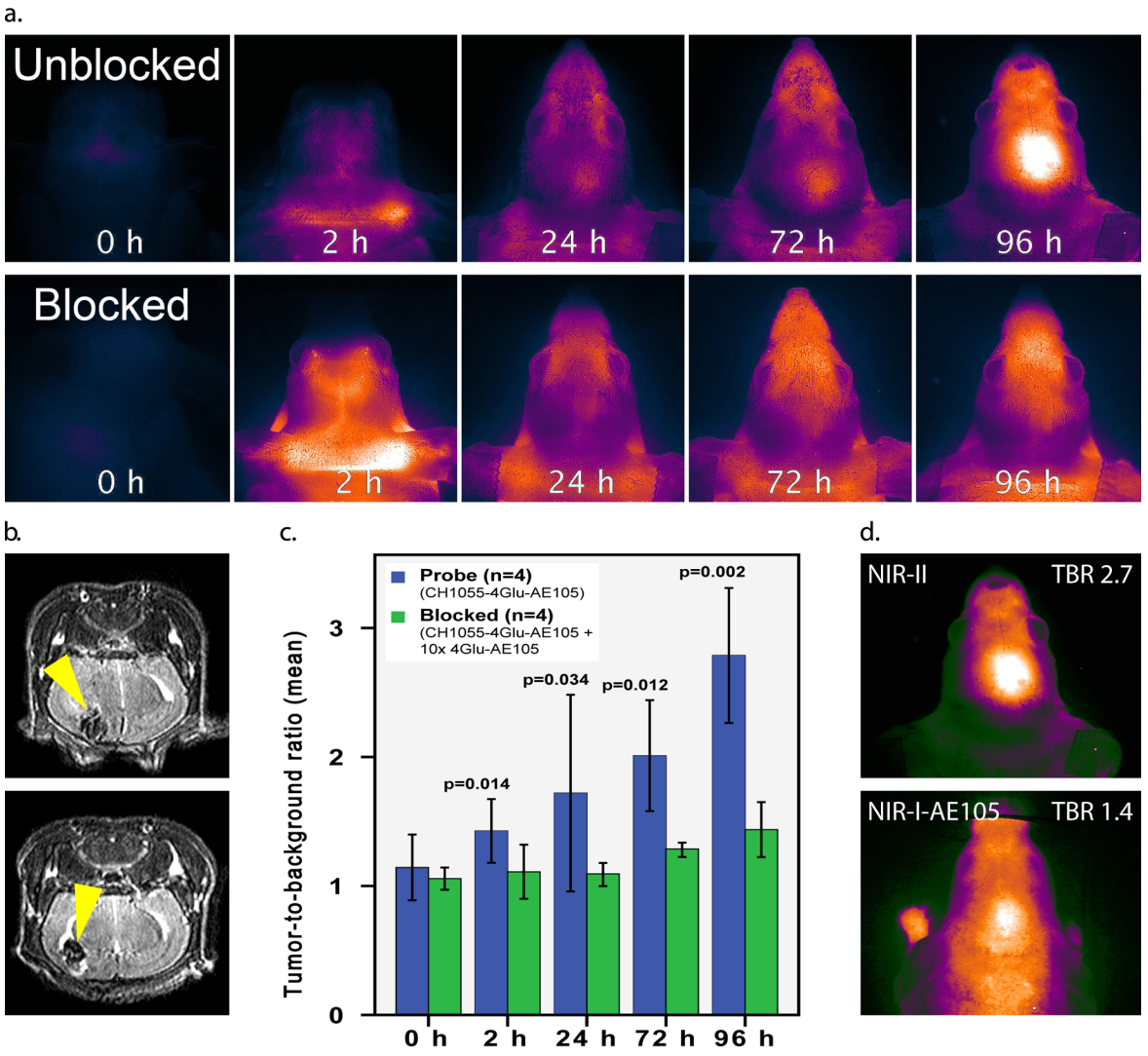

Figure 2. (a) Dynamic imaging of CH1055-4Glu-AE105 in orthotopic GBM models in the unblocked (top images) and blocked (10 times 4Glu-AE105, bottom images) group (n = 4 per group); (b) corresponding MRI with clear tumors (yellow arrows) in both unblocked and blocked mice; (c) quantification analysis of NIR-II images. Mean tumor-to-background ratio over time between blocked (green bars) and unblocked (blue bars) animals; (d) side-to-side comparison between a NIR-I-AE105 probe and the NIR-II probe (CH1055-4Glu-AE105). NIR-I TBR = 1.4 vs NIR-II TBR = 2.7.

background signal of 35,000 Gray) (Figure 3). Additionally, an incomplete resection was performed with a MBR = 1.5 (remaining postoperative fluorescent signal in the periphery/margin with a Gray Value of 52,500 and a background signal of 36,000 Gray) (Figure 3).

Immunohistochemistry. Immunohistochemistry evaluation of the tumor resected mice showed a positive (black) staining at the margin of the incomplete resection (blue arrows in Figure 3b). Contrarily, there was no positive staining at the margin of the complete resection (Figure 3a).

Biodistribution, Toxicity, and Plasma Stability. Biodistribution assessment showed accumulation of the probe primarily in the liver and the normalized intensities for major organs were liver = 1.00 (reference value), small intestines = 0.35, kidneys = 0.18, colon = 0.14, spleen = 0.12, lungs = 0.11, ventricle = 0.10, and heart = 0.08 (Figure 4a,b).

The probe was stable within the relevant time window with normalized area under curve (AUC) values of 67% intact probe after 24 h and 60% after 5 days (Figure 4c).

All mice tolerated the treatment well and showed no signs of abnormal behavior and/or clinical symptoms of toxicity during the entire observation period (5 days). The biodistribution determined that the liver receives the highest dose of probe and was consequently collected at the end of the study for pathological examination. Stained liver sections were examined and showed a preserved structure with no signs of inflammation, abnormal pigmentation, induction in the cytoplasm, steatosis, bleeding, or major areas with necrosis (Figure 5). Enlarged nuclei with changed chromatin structure were observed in some areas and is attributed to delayed fixation from euthanasia to formalin fixation. Single necrotic cells/cell debris were present focally in the sinusoidal space along with hepatocytes in mitosis (Figure 5b). These changes are nonspecific and commonly seen and cannot be attributed to toxic effects. Additionally, no accumulation of macrophages was found as evidence of eradication after hepatocyte damage. Overall, there is no pathological evidence for a hepatotoxic effect of the probe.

DOI: 10.1021/acs.bioconjchem.8b00669
Bioconjugate Chem. 2018, 29, 3833−3840

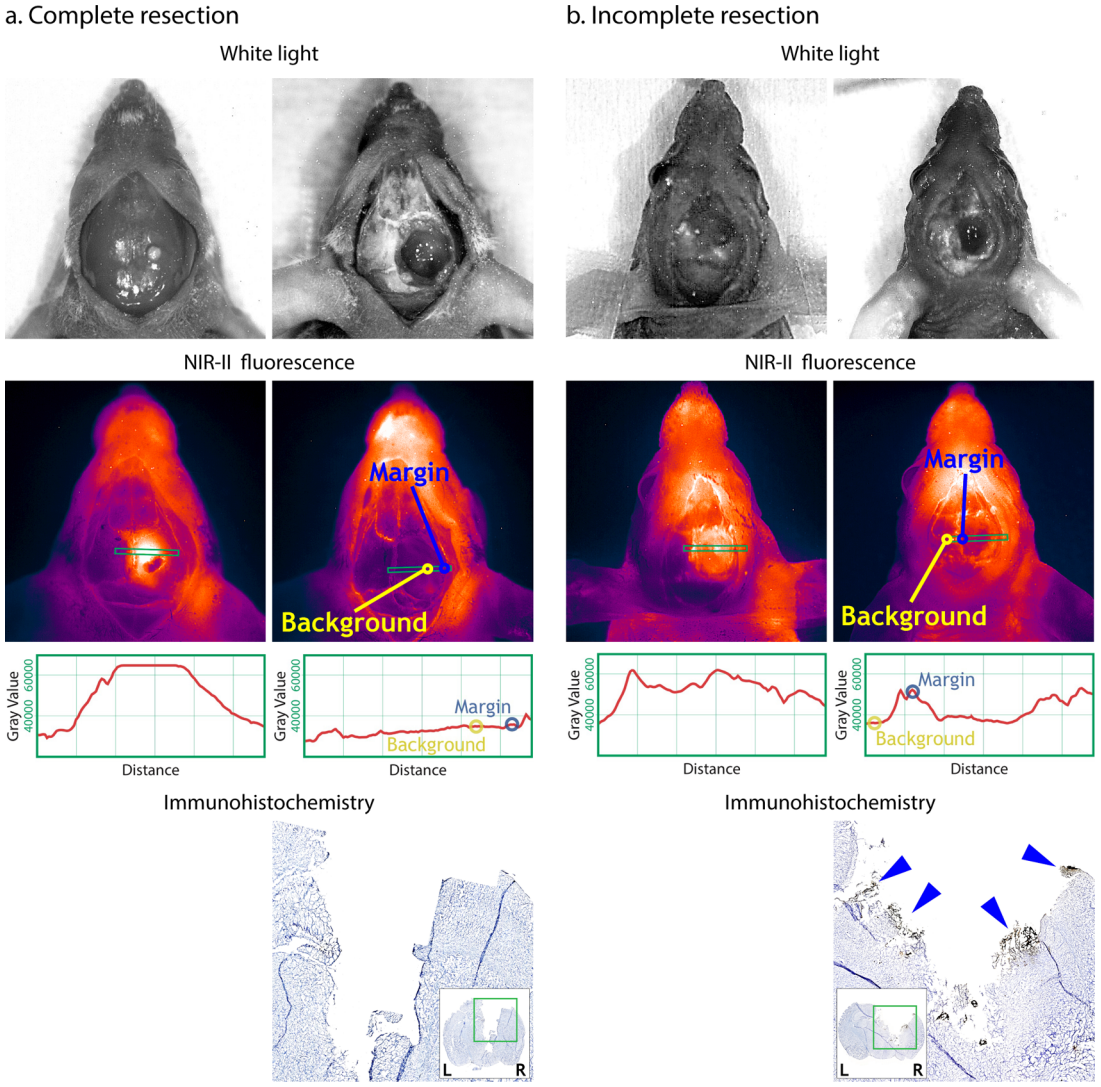

Figure 3. For both Complete resection (a) and Incomplete resection (b), left-hand side pictures are taken prior to tumor resection and right-hand side pictures are after resection. Complete resection: no signal left around the tumor at the postoperative NIR-II picture and it is considered a complete resection. Yellow circle indicates the margin (M = 36,000 Gray Value) and the blue circles indicates the tumor free background signal (B = 35,000 Gray Value) resulting in a margin-to background ratio = 1.0. Incomplete resection: clear signal at the tumor margin at the postoperative picture indicating positive resection margins. Yellow circle indicates the positive margin (M = 52,500 Gray Value) and the blue circles indicates the tumor free background signal (B = 35,000 Gray Value) resulting in a margin-to-background ratio = 1.5. On ICH, blue arrows are pointing at uPAR positive stained tumor cells.

DISCUSSION

GBM holds major challenges in obtaining negative resection margins due to the irregular border and difficulties in distinguishing cancerous tissue from healthy tissue. Accordingly, new tools are needed for guiding surgeons and optical imaging is such a tool.

We already have a well-tested small peptide ligand, AE105, targeting uPAR. The use of a small peptide ligand may be particularly well-suited for intraoperative optical imaging due to the relatively short plasma half-life, compared to, e.g., antibodies, allowing for administration shortly before the surgery is started, possibly concurrent with induction of anesthesia. Antibody based probes, in contrast, circulate for a long time in the blood limiting the clinical usefulness due to high background signal leading to low TBR. Although this could be circumvented by early administration, days prior to surgery, it is rather impractical from a clinical point of view.

Proof-of-concept for uPAR targeted NIR-I (ICG-labeled AE105) imaging has previously been established by us in GBM and HNSCC.[15,17] The ICG-AE105 clearly visualized the tumors although within the limitations of the NIR-I window. We have therefore now successfully synthesized a small peptide based probe consisting of a targeting peptide and a small molecule fluorophore within the superior NIR-II window. The probe showed a clear delineation of the tumor with a through-skull TBR of as high as 2.7 and presumably even higher when the skin and the skull are removed ensuring necessary precision and contrast to achieve negative resection margins. When we performed the resection, we experienced an increase in signal in and around the skin incision and at the edges of the skull hole for unknown reasons (Figure 2 compared to Figure 3). Additionally, we saw high signals in the snout of the mice compared to the rest of the body. Due to the proximity to the brain and tumor in such small animals this phenomenon possibly increases the background noise around the tumor. In

DOI: 10.1021/acs.bioconjchem.8b00669
Bioconjugate Chem. 2018, 29, 3833−3840

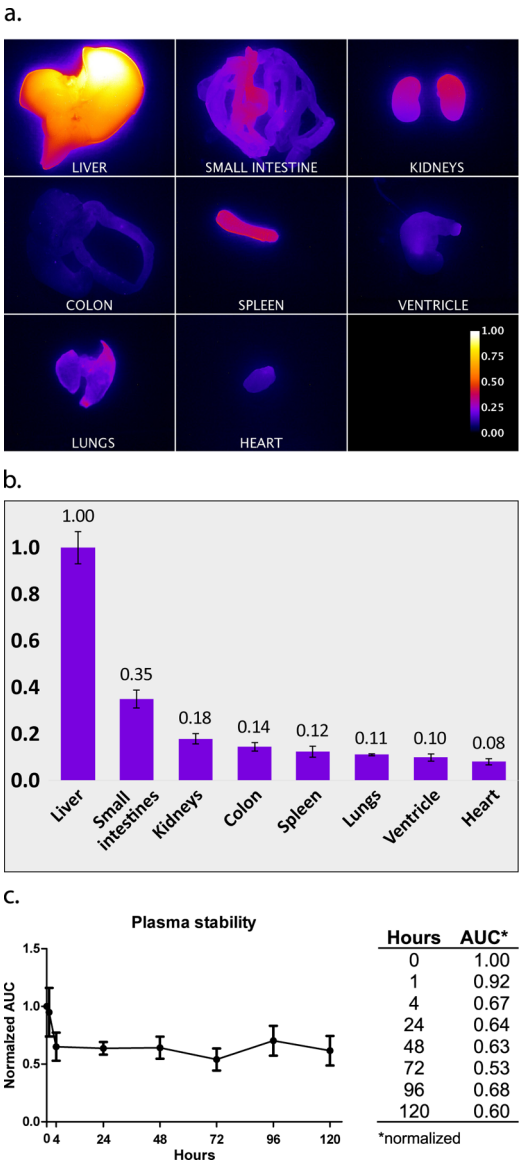

Figure 4. Biodistribution of CH1055-4Glu-AE105. (a) Visual distribution of signal intensity (normalized) for major organs; (b) normalized quantification of the signal (n = 2); (c) plasma stability curve and table with normalized area under curve (AUC) (0 h as reference).

humans, this phenomenon might or might not arise, but the distance is greater between the nasal area and the brain tumor and would probably circumvent the issue resulting in less background signal.

Our study shows that CH1055-4Glu-AE105 based NIR-II FLI allows real-time in vivo intraoperative visualization in living animals and can guide the surgeon to identify and resect fluorescent tissue while sparring adjacent nonfluorescent tissue. As evaluated with IHC, there is a clear compliance between the intraoperative fluorescent signal at the margins and the IHC staining. The NIR-II technology allows detection of very small amounts of tumor tissue comprising relatively few cells and can guide the surgeon to resect this tissue until no signal is left indicating that there is no tumor tissue meaning a complete resection with negative margins. Orthotopic GBM models increasingly comprise patient derived xenografts. The advantage of patient derived orthotropic models (PDOX) is that they

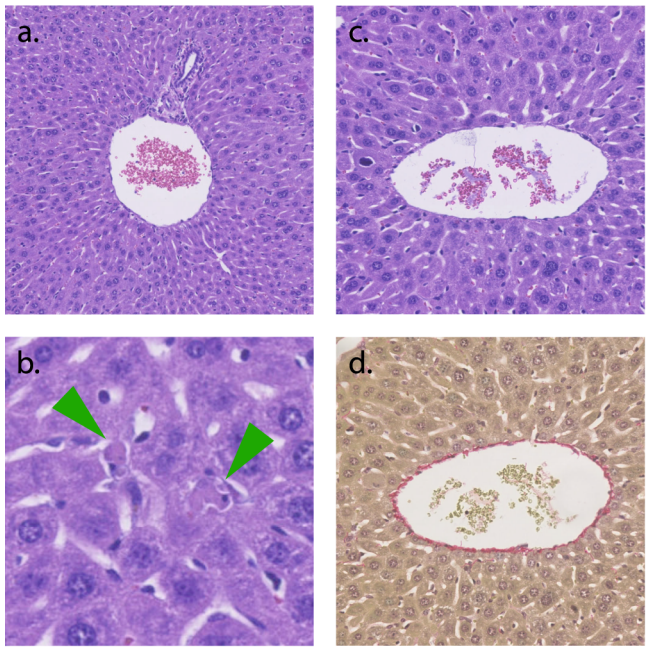

Figure 5. Special stained liver. (a) portal triad, HE staining; (b) liver parenchyma with apoptotic hepatocytes (arrows), HE staining; (c) central vein, HE staining; (d) central vein, modified Sirius connective tissue staining.

combine more realistic tumor composition with the effect of the tumor microenvironment. This probably leads to a more realistic model regarding single cell invasions. Single cell invasion is a challenge in patients and identification and visualization of these cells is important and a goal of our methodology. Therefore, in future studies it might be considered to include PDOX.

In addition to GBM and cancer targeted FLI, the NIR-II FLI technology with increased imaging depth might be applied for through-skin imaging of varies superficial healthy and non-healthy tissues, e.g., cutaneous and subcutaneous lesions, peripheral nervous tissue, and superficial vessels. Visualization of deeper structures are still limited even with the NIR-II FLI, and therefore recent advantages with molecular targeted probes have been moving toward multimodal probes combining different imaging modalities (CT/MR/photoacoustic US/FLI) and treatment therapies (chemo/photothermal) to circumvent the limitations on penetration, spatial, and temporal resolution of each modality alone.[26,27]

The probe and imaging setup has shown promising preclinical results and holds translational potential. We might consider applying our current findings to humans to study the potential and ultimately increase survival.

EXPERIMENTAL PROCEDURES

Probe Synthesis and Characterization. A targeted NIR-II fluorescent probe was developed by conjugating an in-house synthesized NIR-II fluorophore, CH1055, and a uPAR targeting small peptide 4Glu-AE105. Solid phase peptide synthesis of the N-terminal glutamic acid extended AE105 peptide (4Glu-AE105-NH_2) was performed by the Fmoc strategy on a Rink amide resin bed and subsequently conjugated with the NIR-II fluorophore CH1055 made in-house as previously described.[13] The probe was purified by reverse phase high performance liquid chromatography (rp-

DOI: 10.1021/acs.bioconjchem.8b00669
Bioconjugate Chem. 2018, 29, 3833−3840

HPLC) on a C4 semiprep column with the mobile phase of solvent A: 0.1% trifluoroacetic acid (TFA) in H_2O and solvent B: 0.1% TFA in acetonitrile. A gradient was performed with solvent B starting at 5% increasing to 95% over 20 min. The product was lyophilized and stored at −80 °C until use. The product was verified by MALDI-TOF-MS, and the purity of the probe was evaluated by analytical HPLC on a C4 column with same setup as above.

Optical properties of the fluophore (CH1055) were performed as described previously.[13]

Affinity. Recombinant human uPAR^{wt} and recombinant human pro-uPA^{S356A} (active-site mutation causing catalytic inactivity) were expressed by *Drosophila* S2-cells and purified as described previously.[28]

The IC_{50}-value of the probe on the uPAR•uPA interaction was determined by surface plasmon resonance (SPR) technology carried out on a Biacore T200 instrument. Initially, pro-uPA^{S356A} was immobilized on a CM5 chip via amine coupling (immobilizing >5000 RU corresponding to ∼0.1 pmol pro-uPA/mm^2). This very high surface density of pro-uPA enforces a heavily mass transport limited reaction rendering the observed association rates (ν_{obs}) directly proportional to the concentrations of binding active uPAR in solution—when low concentrations of uPAR are tested (0.06−2 nM). Subsequently, the experiment was carried out by measuring ν_{obs} of a fixed uPAR concentration (2 nM) in the presence of a 3-fold dilution series of CH1055-4Glu-AE105 ranging from 0.014 nM to 0.28 μM. A standard curve was measured in parallel with a 2-fold dilution series of uPAR ranging from 0.06 nM to 2 nM followed by one repeated concentration point to ensure an unchanged R_{max} value, which validates the biological integrity of the sensor chip. The inhibition profile could be derived from the obtained ν_{obs} in correlation to the standard curve and thus determine the IC_{50} value. Experiments were conducted at 20 °C with a flow rate of 50 μL/min with 300 s association time. The running buffer contained 10 mM HEPES, 150 mM NaCl, 3 mM EDTA, and 0.05% (v/v) surfactant P20, pH 7.4. In between cycles the sensor chip was regenerated with two injections of 0.1 M acetic acid, 0.5 M NaCl.

Cell Line and Culturing. All cells were cultured in Dulbecco's Modified Eagle's medium (DMEM) added 10% fetal bovine serum (FBS) and 1% Penicillin-Streptomycin at 37 °C in humid 5% CO_2 air and passaged or harvested when reaching 80−90% confluency. Human GBM cells (U87MG) were obtained from American Type Culture Collection (Manassas, VA).

Animal Models. All experimental procedures involving animals were approved by the Stanford University Institutional Animal Care and Use Committee. The animals were anesthetized with 2−3% isoflurane prior to any procedure. 6−12-week-old female nude mice (strain: nu/nu; Charles River Laboratories, USA) were orthotopically xenografted with U87MG (n = 8).

The orthotopic GBM tumor model was established by inoculating 4.00×10^5 U87MG cells suspended in 4 μL of ice-cold phosphate buffered saline (PBS, pH 7.4, 10 mM) in the right hemisphere, 2 mm anterior and 2 mm lateral to the lambda at 3 mm depth held in place with a stereotactic frame (Stoelting, Wood Dale, IL). The cells were injected over 5 min with a blunt-ended Hamilton syringe kept in place for further 1 min before retraction at a speed of 1 mm per 10 s. Tumor growth was subsequently monitored by MRI (3 T) by axial T_2-weighted imaging. When the tumor was visible and had a midline deviation, the animal was included in the fluorescence imaging protocol.

Fluorescence Imaging. The characteristics of the probe were evaluated at the Stanford Canary Center Preclinical Imaging Facility by a customized fluorescence imaging setup. The signal was generated by exciting the probe with an 808 nm laser and the emission in the NIR-II window was acquired by a NIRvana 640 (Princeton Instruments) through a 1050 nm cutoff filter. To characterize the *in vivo* biodistribution and tumor imaging properties, CH1055−4Glu-AE105 (40 nmol) was administered through tail vein injection into all the GBM bearing mice (n = 8). In addition, a blocking dose of 10× 4Glu-AE105 (400 nmol) was injected in half of the animals (n = 4) to assess the *in vivo* targeting specificity to uPAR. Dynamic imaging was performed with data acquisition at 0, 2, 4, 6, and 24 h after injection and then daily until tumor resection.

Surgical Procedure. Anesthetized animals where disinfected at the scalp prior to a midline incision reaching from the level of the eyes and approximately 2 cm caudal. The periost was ruptured and removed with a cotton swap with ethanol and access to the brain through the exposed skull was obtained through a circular craniotomy measuring approximately 6−7 mm in diameter performed with a surgical drill. Resection of brain tissue was performed with a 18G cannula on a syringe connected to vacuum. The tumor tissue was removed stepwise by visualizing the fluorescent tissue with the NIR-II camera, then removing some of the identified tissue and reevaluating the remaining fluorescent tissue with the NIR-II camera. This cycle was repeated until there was no remaining signal. Visualization was performed in a cabinet with the camera and excitation laser fixed at the top. The mice were visualized inside the cabinet and taken out under a surgical microscope for resection guided by the image on the monitor. This procedure was performed successively until no signal was left. Occasionally, the mice had resections inside the cabinet under direct guidance of the image (mainly when very little signal was left). The imaging could be performed with ambient/visible light from LEDs placed inside the cabinet. After surgery, the midline incision was closed with tissue adhesive (Vetbond, 3M, Minnesota, USA). For biodistribution, unblocked mice (n = 2) were sacrificed and the major organs dissected for absolute/unweighted signal intensity quantification.

Plasma Stability. Plasma from three mice was collected and pooled. The probe was incubated in 100 μL plasma at same probe/plasma ratio as when performing the imaging (2.5 mL plasma in a nude mouse) and stored at 37 °C for 0 h, 1, 4, 24, 48, 72, 96, and 120 h. All samples were added 100 μL acetonitrile for protein precipitation and centrifuged for 5 min at 10,000 G. The supernatant was collected and run through analytical HPLC as described above. Area under curve (AUC) at 790 nm at the known retention time for the intact probe was used for each time point and normalized to AUC at 0 h. Three samples were analyzed for each time point.

Immunohistochemistry. Immunohistochemistry (IHC) was used to evaluate the correspondence between NIR-II signal and cancer cells. The brain tissue was coronally sectioned in serial and O.C.T. was removed with Histo-clear II (National diagnostics, England) and ethanol. Thereafter, tissue was pretreated with proteinase K (Agilent, California) for 6 min. The staining was performed with an in-house

DOI: 10.1021/acs.bioconjchem.8b00669
Bioconjugate Chem. 2018, 29, 3833−3840

antibody, poly rabbit-anti-human-uPAR, from Finsen laboratory. The stained slides were imaged with a Zeiss Axio Scan Z1 slide scanner.

Liver toxicology was carried out at Department of Pathology, Rigshospitalet, Denmark and all histology sections were evaluated by a skilled chief physician subspecialized in gastrointestinal pathology.

AUTHOR INFORMATION

Corresponding Authors

*E-mail: zcheng@stanford.edu. Phone: 650-723-7866. Fax: 650-736-7925.

*E-mail: akjaer@sund.ku.dk.

ORCID

Sorel Kurbegovic: 0000-0002-5717-2271

Zhen Cheng: 0000-0001-8177-9463

Notes

The authors declare no competing financial interest.

ACKNOWLEDGMENTS

This work was supported, in part, by the Office of Science (BER), U.S. Department of Energy (DE-SC0008397), a grant from the Lundbeck Foundation to Stanford University to fund the DARE fellowship (Danish American Research Exchange) for Sorel Kurbegovic in 2016−2017, the European Union's EU Framework, Programme for Research and Innovation Horizon 2020, the European Research Council (ERC) under the European Union's Horizon 2020 research and innovation programme (grant agreement No 670261), the Lundbeck Foundation, the Novo Nordisk Foundation, the Innovation Fund Denmark, the Neye Foundation, the Research Council for Independent Research, Righospitalet Research Council and the Research Fund of the Capital Region of Denmark. The brain surgery was kindly assisted by Klara Holm. Pathological evaluation was kindly provided by Jane Preuss Hasselby and Gro Linno Willemoe, Department of Pathology, Rigshospitalet, Denmark.

ABBREVIATIONS

5-ALA, 5-aminolevulinic acid; AUC, area under curve; CT, computed tomography; DMEM, Dulbecco's Modified Eagle's medium; FBS, fetal bovine serum; FDA, Food and Drug Administration; FLI, fluorescence imaging; GBM, glioblastoma; HNSCC, head and neck squamous cell carcinoma; ICG, indocyanine green; IHC, immunohistochemistry; MALDI-TOF-MS, matrix assisted laser desorption ionization-time-of-flight mass spectrometry; MBR, margin-to-background ratio; MRI, magnetic resonance imaging; MW, molecular weight; NIR-I, first near-infrared window; NIR-II, second near-infrared window; PDOX, patient derived orthotropic models; TBR, tumor-to-background ratio; TFA, trifluoroacetic acid; uPAR, urokinase plasminogen activator receptor

REFERENCES

(1) Kelly, C., Majewska, P., Ioannidis, S., Raza, M. H., and Williams, M. (2017) Estimating progression-free survival in patients with glioblastoma using routinely collected data. *J. Neuro-Oncol. 135*, 621.

(2) Almeida, J. P., Chaichana, K. L., Rincon-Torroella, J., and Quinones-Hinojosa, A. (2015) The value of extent of resection of glioblastomas: clinical evidence and current approach. *Curr. Neurol. Neurosci. Rep. 15*, 517.

(3) Stummer, W., Reulen, H. J., Meinel, T., Pichlmeier, U., Schumacher, W., Tonn, J. C., Rohde, V., Oppel, F., Turowski, B., Woiciechowsky, C., et al. (2008) Extent of resection and survival in glioblastoma multiforme: identification of and adjustment for bias. *Neurosurgery 62*, 564−76 discussion 564−76. .

(4) Ivan, M. E., Yarlagadda, J., Saxena, A. P., Martin, A. J., Starr, P. A., Sootsman, W. K., and Larson, P. S. (2014) Brain shift during bur hole-based procedures using interventional MRI. *J. Neurosurg. 121*, 149−60.

(5) Ohue, S., Kumon, Y., Nagato, S., Kohno, S., Harada, H., Nakagawa, K., Kikuchi, K., Miki, H., and Ohnishi, T. (2010) Evaluation of intraoperative brain shift using an ultrasound-linked navigation system for brain tumor surgery. *Neurol Med. Chir (Tokyo) 50*, 291−300.

(6) Jin, Y., Wang, K., and Tian, J. (2018) Preoperative Examination and Intraoperative Identification of Hepatocellular Carcinoma Using a Targeted Bimodal Imaging Probe. *Bioconjugate Chem. 29*, 1475−1484.

(7) Jin, Y., Yang, X., and Tian, J. (2018) Targeted polypyrrole nanoparticles for the identification and treatment of hepatocellular carcinoma. *Nanoscale 10*, 9594−9601.

(8) Hillary, S. L., Guillermet, S., Brown, N. J., and Balasubramanian, S. P. (2018) Use of methylene blue and near-infrared fluorescence in thyroid and parathyroid surgery. *Langenbecks Arch Surg. 403*, 111.

(9) Diaz, R. J., Dios, R. R., Hattab, E. M., Burrell, K., Rakopoulos, P., Sabha, N., Hawkins, C., Zadeh, G., Rutka, J. T., and Cohen-Gadol, A. A. (2015) Study of the biodistribution of fluorescein in glioma-infiltrated mouse brain and histopathological correlation of intraoperative findings in high-grade gliomas resected under fluorescein fluorescence guidance. *J. Neurosurg. 122*, 1360−9.

(10) Eyupoglu, I. Y., Hore, N., Fan, Z., Buslei, R., Merkel, A., Buchfelder, M., and Savaskan, N. E. (2015) Intraoperative vascular DIVA surgery reveals angiogenic hotspots in tumor zones of malignant gliomas. *Sci. Rep. 5*, 7958.

(11) Stummer, W., Stocker, S., Wagner, S., Stepp, H., Fritsch, C., Goetz, C., Goetz, A. E., Kiefmann, R., and Reulen, H. J. (1998) Intraoperative detection of malignant gliomas by 5-aminolevulinic acid-induced porphyrin fluorescence. *Neurosurgery 42*, 518−25 discussion 525−6. .

(12) Antaris, A. L., Chen, H., Diao, S., Ma, Z., Zhang, Z., Zhu, S., Wang, J., Lozano, A. X., Fan, Q., Chew, L., et al. (2017) A high quantum yield molecule-protein complex fluorophore for near-infrared II imaging. *Nat. Commun. 8*, 15269.

(13) Antaris, A. L., Chen, H., Cheng, K., Sun, Y., Hong, G., Qu, C., Diao, S., Deng, Z., Hu, X., Zhang, B., et al. (2016) A small-molecule dye for NIR-II imaging. *Nat. Mater. 15*, 235−42.

(14) Hong, G., Lee, J. C., Robinson, J. T., Raaz, U., Xie, L., Huang, N. F., Cooke, J. P., and Dai, H. (2012) Multifunctional in vivo vascular imaging using near-infrared II fluorescence. *Nat. Med. 18*, 1841−6.

(15) Juhl, K., Christensen, A., Persson, M., Ploug, M., and Kjaer, A. (2016) Peptide-Based Optical uPAR Imaging for Surgery: In Vivo Testing of ICG-Glu-Glu-AE105. *PLoS One 11*, e0147428.

(16) Persson, M., Nedergaard, M. K., Brandt-Larsen, M., Skovgaard, D., Jorgensen, J. T., Michaelsen, S. R., Madsen, J., Lassen, U., Poulsen, H. S., and Kjaer, A. (2016) Urokinase-Type Plasminogen Activator Receptor as a Potential PET Biomarker in Glioblastoma. *J. Nucl. Med. 57*, 272−8.

(17) Christensen, A., Juhl, K., Persson, M., Charabi, B. W., Mortensen, J., Kiss, K., Lelkaitis, G., Rubek, N., von Buchwald, C., and Kjaer, A. (2017) uPAR-targeted optical near-infrared (NIR) fluorescence imaging and PET for image-guided surgery in head and neck cancer: proof-of-concept in orthotopic xenograft model. *Oncotarget*, 1 DOI: 10.18632/oncotarget.14282.

(18) He, C., He, P., Liu, L. P., and Zhu, Y. S. (2001) Analysis of expressions of components in the plasminogen activator system in high- and low-metastatic human lung cancer cells. *J. Cancer Res. Clin. Oncol. 127*, 180−6.

(19) Hofmann, R., Lehmer, A., Buresch, M., Hartung, R., and Ulm, K. (1996) Clinical relevance of urokinase plasminogen activator, its receptor, and its inhibitor in patients with renal cell carcinoma. *Cancer 78*, 487−92.

DOI: 10.1021/acs.bioconjchem.8b00669
Bioconjugate Chem. 2018, 29, 3833−3840

(20) Foekens, J. A., Peters, H. A., Look, M. P., Portengen, H., Schmitt, M., Kramer, M. D., Brunner, N., Janicke, F., Meijer-van Gelder, M. E., Henzen-Logmans, S. C., et al. (2000) The urokinase system of plasminogen activation and prognosis in 2780 breast cancer patients. *Cancer Res. 60*, 636−43.
(21) Persson, M., and Kjaer, A. (2013) Urokinase-type plasminogen activator receptor (uPAR) as a promising new imaging target: potential clinical applications. *Clin. Physiol. Funct. Imaging 33*, 329−37.
(22) Romer, J., Nielsen, B. S., and Ploug, M. (2004) The urokinase receptor as a potential target in cancer therapy. *Curr. Pharm. Des. 10*, 2359−76.
(23) Jorgensen, T. J., Gardsvoll, H., Dano, K., Roepstorff, P., and Ploug, M. (2004) Dynamics of urokinase receptor interaction with Peptide antagonists studied by amide hydrogen exchange and mass spectrometry. *Biochemistry 43*, 15044−57.
(24) Persson, M., Skovgaard, D., Brandt-Larsen, M., Christensen, C., Madsen, J., Nielsen, C. H., Thurison, T., Klausen, T. L., Holm, S., Loft, A., et al. (2015) First-in-human uPAR PET: Imaging of Cancer Aggressiveness. *Theranostics 5*, 1303−16.
(25) Skovgaard, D., Persson, M., Brandt-Larsen, M., Christensen, C., Madsen, J., Klausen, T. L., Holm, S., Andersen, F. L., Loft, A., Berthelsen, A. K., et al. (2017) Safety, Dosimetry, and Tumor Detection Ability of (68)Ga-NOTA-AE105: First-in-Human Study of a Novel Radioligand for uPAR PET Imaging. *J. Nucl. Med. 58*, 379−386.
(26) Jin, Y., Ma, X., Zhang, S., Meng, H., Xu, M., Yang, X., Xu, W., and Tian, J. (2017) A tantalum oxide-based core/shell nanoparticle for triple-modality image-guided chemo-thermal synergetic therapy of esophageal carcinoma. *Cancer Lett. 397*, 61−71.
(27) Wang, Q., Yan, H., Jin, Y., Wang, Z., Huang, W., Qiu, J., Kang, F., Wang, K., Zhao, X., and Tian, J. (2018) A novel plectin/integrin-targeted bispecific molecular probe for magnetic resonance/near-infrared imaging of pancreatic cancer. *Biomaterials 183*, 173−184.
(28) Gardsvoll, H., Jacobsen, B., Kriegbaum, M. C., Behrendt, N., Engelholm, L., Ostergaard, S., and Ploug, M. (2011) Conformational regulation of urokinase receptor function: impact of receptor occupancy and epitope-mapped monoclonal antibodies on lamellipodia induction. *J. Biol. Chem. 286*, 33544−56.

DOI: 10.1021/acs.bioconjchem.8b00669
Bioconjugate Chem. 2018, 29, 3833−3840